arXiv:1407.3025v1 [astro-ph.HE] 11 Jul 2014

submitted to ApJ, on July 14, 2014

The optical variability of SDSS quasars from multi-epoch spectroscopy: I. Results from 60 quasars with $\geq$ six-epoch spectra

Hengxiao Guo (郭恒潇)[1,2], Minfeng Gu[1]
[1]Key Laboratory for Research in Galaxies and Cosmology, Shanghai Astronomical Observatory, Chinese Academy of Sciences, 80 Nandan Road Shanghai 200030, China
[2] University of Chinese Academy of Sciences, 19A Yuquanlu, Beijing 100049, China;
hxguo@shao.ac.cn, gumf@shao.ac.cn

ABSTRACT

In a sample of 60 quasars selected from Sloan Digital Sky Survey (SDSS) with at least six-epoch spectroscopy, we investigate the variability of emission lines and continuum luminosity at various aspects. A strong anti-correlation between the variability and continuum luminosity at 2500 Å is found for the sample, which is consistent with previous works. In individual sources, we find that half of the sample objects have a trend of being bluer-when-brighter trend (BWB), while the remaining half exhibit redder-when-brighter trend (RWB). Although the mechanism for RWB is unclear, the effects of host galaxy contribution due to seeing variations can not be completely ruled out. As expected from photoionization model, the positive correlations between the broad emission line and continuum luminosity are found in most individual sources, as well as for the whole sample. We confirm the Baldwin effect in most individual objects and the whole sample, while a negative Baldwin effect is also found in several quasars, which can be at least partly (if not all) due to the host galaxy contamination. We find positive correlations between the broad emission line luminosity and line width in most individual quasars, as well as the whole sample, implying a more variable line base than the line core.

Subject headings: galaxies: active – quasars: general – techniques: spectroscopic

1. Introduction

Active Galactic Nuclei (AGNs) are characterized by variability at almost all wavelengths (Ulrich et al. 1997). Investigating the variability is a very important approach to probe the physical

properties of AGNs. There have been many systematic studies on the variability of AGNs by using photometric data, although such measurements are subject to the line contributions in the photometric bands (e.g. Vanden Berk et al. 2004). Several interesting results have been obtained from various AGN samples. The well-known anti-correlation between the variability and continuum luminosity was firstly discovered by Angione & Smith (1972), and later, it was confirmed by many other works (Hook et al. 1994; Wilhite et al. 2008; Zuo et al. 2012). Although there are other possibilities for explaining this result (Cid Fernandes et al. 2000), Li & Cao (2008) explained that the anti-correlation could be qualitatively explained by the standard accretion disc model assuming the variability was caused by the change of accretion rate.

A positive correlation was found between the variability and redshift (e.g., Trevese et al. 1994; Hook et al. 1994; Cid Fernandes et al. 1996), which was later confirmed in a sample of over 25,000 SDSS quasars (Vanden Berk et al. 2004; Zuo et al. 2012). The correlation can be caused by the variability - wavelength relation (Cristiani et al. 1996), which is likely related with the variability mechanism (Vanden Berk et al. 2004). The positive relation between the optical-UV variability and black hole mass was first reported by Wold et al. (2007), which can be explained by the fact that the more massive black holes were gasless, and produce larger flux variations because they do not have a steady inflow of gaseous fuel. Alternatively, Li & Cao (2008) argued that this relation could be triggered by the change of the accretion rate in their accretion disc model.

Mostly because the spectroscopic observations are time-consuming, there are only a few investigations on the variability of AGNs from multi-epoch spectroscopy, which either focused on reverberation mapping analysis for extensively monitored sources (e.g., Kaspi et al. 2000), or were based on spectroscopic observations at a few epochs (e.g., Wilhite et al. 2005). However, multi-epoch spectroscopy has advantages compared to photometric data. The continuum can be well constrained by excluding the emission line contamination, and the spectral shape can be measured by carefully fitting the continuum on a wide wavelength coverage. Moreover, the line measurements can be obtained, which enable us to study the variability of emission lines.

There have been extensive investigations on the quasar spectral shape, Baldwin effect and line width (e.g., Fan et al. 1998; Gu & Ai 2011a,b,b; Wu et al. 2005; Zuo et al. 2012; Baldwin 1977; Wills et al. 1993; Wilhite et al. 2005). The bluer-when-brighter trend (BWB) is very common in AGNs, however the redder-when-brighter trend (RWB) has also been found, for example, in a sample of 544 quasars with two-epoch spectroscopy (Bian et al. 2012a). The anti-correlation between the emission line equivalent width (EW) and the continuum luminosity, so-called the Baldwin Effect (Baldwin 1977) was originally found in the broad emission lines in UV/optical band (see Shields 2007, for a review), and was also detected in narrow lines (e.g., Zhang et al. 2013). Recently, a strong Baldwin effect for C IV and Mg II and a week negative Baldwin effect for Hβ were presented by Shen et al. (2011) for DR7 quasar catalog. There is still no definitive conclusion on

the correlation between the emission line luminosity and the line width. A negative correlation was found by Wills et al. (1993) in a sample of 123 quasars with single-epoch spectroscopy, while a positive correlation was discovered by Wilhite et al. (2005) based on a sample of 315 quasars with two-epoch spectroscopy. We note that all these works focused on studies of entire samples; not much work has been done for individual quasars. Moreover, usually only two-epoch spectroscopy was used in individual sources. To further study the Baldwin effect, the variability of the spectral shape and line width, especially in individual objects, the quasar samples with multi-epoch spectroscopy data are needed.

In this paper, we investigate the quasar variabilities by constructing a sample of quasars with multi-epoch spectroscopy from Sloan Digital Sky Survey (SDSS) [1] (Abazajian et al. 2009; Ahn et al. 2012). The multi-epoch spectroscopic data enables us not only to study the continuum variability, but also the effects that involve line variations relative to the continuum and relative to the line width, for both individual quasars and whole sample. In order to increase the probability of detecting variabilities, and to improve correlation analysis for individual QSOs, the quasars with at least six-epoch spectroscopy were selected. In Section 2, we describe the quasar sample, and the spectroscopic data analysis is given in Section 3. We show the results, and discussions in Sections 4, and 5, respectively. Finally, our conclusions are drawn in Section 6. Throughout the paper, a cosmology with H_0 = 70 km s^{-1} Mpc^{-1}, $\Omega_{\rm m}$ = 0.3 and Ω_Λ = 0.7 is adopted, and the spectral index α_λ is defined as $f_\lambda \propto \lambda^{\alpha_\lambda}$ with f_λ being the flux density at wavelength λ.

2. Sample

The SDSS data release seven (DR7) quasar catalog consists of 105,783 quasars selected as brighter than $M_{\rm i}$ = -22.0 and to have at least one broad emission line with FWHM larger than 1000 km s^{-1} (Schneider et al. 2010). These quasars were selected for spectroscopic observation according to the quasar target selection algorithm (Richards et al. 2002; Schneider et al. 2010), which selects objects with $i < 19.1$ (for *i*-band apparent magnitude *i*) and their nonstellar colors similar to redshift ≤ 3 quasars, and unresolved objects with $i < 20.2$ and colors similar to higher-redshift quasars. Moreover, all $15 < i < 19.1$ unresolved sources within 2" of a FIRST radio detection were also chosen.

The spectral wavelength coverage is 3,800Å - 9,200Å with the spectral resolution R $\sim$ 1,850 - 2,200, and the five-band *u,g,r,i,z* magnitudes have typical errors of about 0.03 mag. A comprehensive compilation of quasar properties is presented for DR7 quasars in Shen et al. (2011),

[1] `http://dr9.sdss3.org/bulkSpectra`

including the continuum and emission line measurements, black hole masses, and radio properties etc.. To study the variabilities, the quasars with at least two-epoch spectroscopic observations were selected by searching the number of spectroscopic observations given in Shen et al. (2011), which results in a sample of 7,063 quasars. The multi-epoch spectroscopic observations are mainly from the overlap survey areas between adjacent plates, and sometimes were used to monitor the system (Dawson et al. 2013). As the first of a series papers, we present in this work the results of 60 quasars with at least six-epoch spectroscopic observations. The redshift covers from 0.08 to 3.78 for these 60 objects. Eight quasars have been detected in the Faint Images of the Radio Sky at Twenty Centimeters (FIRST) 1.4-GHz radio survey (Becker et al. 1995). The radio loudness is available for all eight sources in Shen et al. (2011), of which seven objects are radio-loud according to the definition of radio loudness $R = f_{6\mathrm{cm}}/f_{2500} \geq 10$ ($f_{6\mathrm{cm}}$ and f_{2500} are the flux density at rest-frame 6 cm and 2500 Å, respectively). When available, we include in our analysis the spectra from SDSS data release nine (DR9), which is the first spectroscopic data from the SDSS-III Baryon Oscillation Spectroscopic Survey (BOSS) (Ahn et al. 2012). The spectra of DR9 cover a wider wavelength range 3,600 - 10,500 Å than that of DR7. The biggest advantage of our sample is that each of our sample sources have at least six-epoch spectroscopy, therefore, we will mainly focus on the results for individual objects, instead of global sample as our sample size is relatively small compared to previous works.

Since different emission lines are covered in SDSS spectra for sources at different redshift, our sample sources are separately listed in Tables 1 - 3. Table 1 lists the quasars at $z \leq 0.4$, while the objects at $0.4 < z \leq 0.8$, and $z > 0.8$ are presented in Tables 2 and 3, respectively.

3. Spectroscopic analysis

The data reduction on the SDSS spectra follows the procedure in Chen et al. (2009), which is illustrated in Fig. 1. After correcting the Galactic extinction with the reddening map of Schlegel et al. (1998), we shifted the spectra to the rest-frame wavelength. In order to obtain reliable line parameters, line-free wavelength ranges were firstly selected as pseudo-continua. In addition to the emission lines, three components are considered: (1) A power-law continuum derived from the emission line-free windows; (2) UV and optical Fe II emission fitted using the templates of Vestergaard & Wilkes (2001) and Véron-Cetty et al. (2004), respectively; (3) A Balmer continuum generated in the same way as Dietrich et al. (2002). The modeling of these three components was performed by minimizing the χ^2 in the fitting process. The final multicomponent fit was then subtracted from the observed spectrum.

The broad emission lines were measured from the continuum subtracted spectra. We mainly focus on several prominent emission lines, i.e., Hα , Hβ , Mg II , and C IV . The Mg II , Hβ

and Hα lines were fitted with two Gaussian components, with one for narrow component with an upper limit of FWHM $\leq$ 1200 km s^{-1}, and the other for broad profile with a lower limit of FWHM $\geq$1200 km s^{-1} (see e.g., Shen et al. 2011). Although it is still unclear whether there is a narrow component, we fitted C IV with two Gaussians.

The blended narrow lines, e.g., [O III] $\lambda\lambda$4959, 5007 and [He II] λ4686 blending with Hβ , and [S II] $\lambda\lambda$6716, 6730, [N II] $\lambda\lambda$6548, 6583 and [O I]λ6300 blending with Hα , are included as one Gaussian component for each line at the fixed line wavelength. The details of spectral analysis were given in Chen et al. (2009). The spectral index of the continuum, the continuum flux, the line width and flux of broad Hα , Hβ , Mg II and C IV lines were obtained from the final fits for our sample, from which the variations of both the continuum and line emission can be investigated for individual sources and whole sample.

4. Results

4.1. The variability in continuum luminosity

The variability of continuum emission is investigated with the rest luminosity at 2500 Å. This wavelength is selected because it is covered in the SDSS spectra for most sources, and the variations at shorter wavelength are known to be larger than longer wavelength (e.g., Cristiani et al. 1997). The luminosity at 2500 Å is directly calculated from the fitted power-law continuum if 2500 Å is covered in the spectrum, otherwise is extrapolated from the power-law continuum, which is the case in seven quasars. We define the continuum variability amplitude for each source as $\Delta\log \lambda L_\lambda = \log \lambda L_{\lambda,\rm max} - \log \lambda {\rm L}_{\lambda,\rm min}$, in which $\lambda L_{\lambda,\rm max}$, and $\lambda L_{\lambda,\rm min}$ are the highest and lowest luminosity at 2500 Å measured from multi-epoch spectra, respectively. To evaluate the significance of variability, two uncertainties are taken into account. The first one is the measurement uncertainties in two involved spectra $\sigma_{\rm s} = \sqrt{\sigma_{\rm s,1}^2 + \sigma_{\rm s,2}^2}$, in which $\sigma_{\rm s,1}$, and $\sigma_{\rm s,2}$ are uncertainties in two spectra. The other is the uncertainties from the power-law fitting $\sigma_{\rm f} = \sqrt{\sigma_{\rm f,1}^2 + \sigma_{\rm f,2}^2}$. The total uncertainty in $\Delta\log \lambda L_\lambda$ is $\sigma = \sqrt{\sigma_{\rm s}^2 + \sigma_{\rm f}^2}$. We found that $\Delta\log \lambda L_\lambda$ is larger than 3σ for all our sources, implying significant continuum variations in our sample. As an example, the continuum variation is shown in Fig. 2 for nine-epoch spectra of SDSS J031003.01-004645.7 (z = 2.115), in which the C IV line variation is also presented.

The relationship between the continuum variability amplitude and various parameters are presented in Fig. 3 for our sample. We find a significant anti-correlation between the continuum variability amplitude and the multi-epoch averaged 2500 Å luminosity with a Spearman rank correlation coefficient $r_{\rm s}$ = –0.38 at $\sim$ 99.7% confidence level (see Fig. 3a). This anti-correlation is

more apparent in binned 2500 Å luminosity. In Fig. 3b, we find a mild anti-correlation between the redshift and the continuum variability amplitude with a Spearman correlation coefficient r_s = –0.27 at $\sim$ 96.6% confidence level. In redshift bins, the continuum variability amplitude decreases with the redshift at $z < 2.5$, while it increases at higher redshift, where however there are only a few objects. For our objects, the variability was obtained from the luminosity at the same rest frame wavelength 2500 Å, which naturally eliminates the selection effect of rest wavelength. However, our result is in contrast to the positive correlations reported in previous works (e.g., Cristiani et al. 1996; Vanden Berk et al. 2004).

By collecting the black hole mass $M_{\rm bh}$ and the Eddington ratio $L_{\rm bol}/L_{\rm Edd}$ from Shen et al. (2011) (see Tables 1 - 3), their relations with the continuum variability amplitude were studied for our sample (see Figs. 3c and 3d). From the Spearman correlation analysis, we failed to find the significant correlation between the continuum variability amplitude and the black hole mass. Similarly, there is no strong correlation between the continuum variability amplitude and the Eddington ratio, although the trend of decreasing variability amplitude with increasing $M_{\rm bh}$ and $L_{\rm bol}/L_{\rm Edd}$ can be seen from the binned values.

In Fig. 3, it can be clearly seen that one quasar (SDSS J022214.38-001745.3, z = 0.773) has much larger variability amplitude than all other objects. In order to evaluate its influence on the correlations, we performed the correlation analysis after excluding the object, and found similar correlation results.

4.2. The spectral variation

The multi-epoch spectroscopic observations enable us to investigate the relationship between the 2500 Å continuum luminosity and the spectral shape (α_λ) for individual sources. The Spearman correlation coefficient and the confidence level are shown for each source in Tables 1 - 3. We find that 30 sources have RWB trend with positive correlations, while the rest of the 30 objects show BWB trend with negative correlation coefficient. While the correlation confidence level is quite low for most objects, we find significant anti-correlations in three quasars at confidence level of $\geq$ 99%, and mild anti-correlations in six objects at 90% $\leq$ p $\leq$ 99% confidence level. In contrast, none of sources have significant positive correlations, and only three quasars have mild positive correlations (SDSS J022518.36-001332.3 at z = 3.63, SDSS J030907.49+002419.0 at z = 2.08, and SDSS J031022.10+004130.0 at z = 0.65, see Tables 2 - 3). The correlations are illustrated in Fig. 4 with two examples, SDSS J030639.57+000343.1 (BWB, r_s = –0.89 at $>$ 99.5%), and SDSS J031022.10+004130.0 (RWB, r_s = 0.67 at $\sim$ 91%).

4.3. Line emission

The correlation between the variations in the broad emission line luminosity with the continuum luminosity is explored for each object, and the results from Spearman correlation analysis are shown in Tables 1 - 3, in which the continuum luminosity at 1350 Å, 3000 Å, 5100 Å, and 5100 Å, correspond to broad C IV , Mg II , Hβ , and Hα lines, respectively.

We find positive correlations between the line and continuum luminosity in most cases (74 of 92 emission lines, $\sim$ 80%), consistent with the photoionization model (Yee 1980), of which $\sim$ 26% (24 of 92) have $\geq$ 90% correlation confidence level. As an example, the correlation between the broad Hα luminosity and the continuum luminosity at 5100 Å is plotted in Fig. 5 for SDSS J030639.57+000343.1. A significant correlation is found with r_s = 0.867 at confidence level of 99.7% (see also Guo & Gu 2014). The linear fit gives

$$\log L_{\mathrm{H}\alpha} = (1.03 \pm 0.13) \log (\lambda L_{\lambda,5100}) - (2.83 \pm 5.81). \quad (1)$$

Interestingly, we find anti-correlations between the line and continuum luminosity in the rest of the cases. However, the anti-correlations are usually very weak (see Tables 1 - 3). Only one object (SDSS J021754.80 +000234.0) exhibits a mild anti-correlation with r_s = –0.77 at $\sim$ 93.0% confidence level (see Table 3), which is shown in Fig. 5 for the broad Mg II luminosity and the continuum luminosity at 3000 Å. The linear fit yields

$$\log L_{\mathrm{MgII}} = (-0.50 \pm 0.32) \log (\lambda L_{\lambda,3000}) + (70.91 \pm 14.66). \quad (2)$$

When putting all multi-epoch line measurements of all our sample sources together, we find significant positive correlations between each line emission and the corresponding continuum luminosity for whole sample (see Fig. 6).

4.4. Baldwin effect

The measurements of emission lines from multi-epoch spectra also enable us to study the Baldwin effect for both individual sources and whole sample. In Tables 1 - 3, we list the Spearman correlation coefficient and corresponding confidence level between the EW (broad C IV , Mg II , Hβ , and Hα) and the continuum luminosity for individual sources. We find that 61 of 92 ($\sim$ 66%) emission lines show anti-correlations, with 13 cases ($\sim$ 14%) at confidence level of $\geq$ 90%. Two sources are found to have significant anti-correlations at confidence level $>$ 99%, i.e., SDSS J031226.12-003708.9 and SDSS J031156.45-004157.0 (see Tables 2 and 3). Strikingly, the positive correlations, namely the negative Baldwin effect, are also found in 31 cases,

however, the correlations are usually weak (confidence level $< 90\%$). The examples of anti-correlation and positive correlation are shown in Fig. 7 for SDSS J031027.82-004950.7 and SDSS J030639.57+000343.1, respectively.

We further study the Baldwin effect for whole sample by plotting all line EW measurements and the corresponding continuum luminosity in Fig. 8. Although the scatter is large, a significant Baldwin effect, i.e., the strong anti-correlation between the line EW and continuum luminosity is found with a Spearman correlation coefficient of $r_s = -0.23$ at $\gg 99.9\%$ confidence level for the broad Mg II line, which is covered in SDSS spectra for most sources.

4.5. Line emission and width

With multi-epoch spectroscopy, we investigate the relationship between the variability of the broad line width FWHM and the broad line luminosity (broad C IV , Mg II , Hβ , and Hα) for individual sources. In Tables 1 - 3, we show the Spearman correlation coefficient and confidence level for various emission lines in each source. While 69 of 92 ($\sim 75\%$) emission lines show a positive correlation, with 24 cases ($\sim 26\%$) at confidence level of $\geq 90\%$, the anti-correlations were also found. Whereas, anti-correlations are usually weak, with only three sources at $> 90\%$ confidence level (C IV in SDSS J022230.28+001844.5, Mg II in SDSS J030911.64+002358.8, and Hα in SDSS J031027.82-004950.7, see Tables 1 - 3). In Fig. 9, the positive and anti-correlation are illustrated with two examples, SDSS J031131.41-002127.4 and SDSS J031027.82-004950.7, for broad C IV , and Hα , respectively.

The relationship between broad line width and luminosity is also explored for whole sample when putting all multi-epoch measurements together (see Fig. 10). The strong correlations are found with Spearman correlation coefficients of 0.14, 0.16, 0.42 and 0.41, all at $> 99\%$ confidence level for C IV , Mg II , Hβ and Hα , respectively. The correlation analysis is not committed for Hα , since only four sources have Hα measurements. In Fig. 10, irrespective of large scatters, the mean values of line FWHM imply that systematically Hβ and Mg II are at similar region, while C IV are relatively closer to central nuclei, with the mean FWHM of 41 Å (~ 7900 km s^{-1}), 48 Å (~ 5100 km s^{-1}), and 90 Å (~ 5500 km s^{-1}) for broad C IV , Mg II , and Hβ , respectively.

5. Discussions

5.1. The color variation

As mentioned in Section 2, the quasars are selected for candidates for spectroscopic observations according to various criterions. While most sources are chosen from their color, some are selected as the detections in FIRST survey. We find that the mean spectral index of all sample $<\alpha_\lambda>=-1.37\pm0.18$ is generally consistent with that of the composite spectrum (α_ν = –0.44, Vanden Berk et al. 2001), which indicates no severe reddening for whole sample. There are 15 quasars with $i > 19.1$ (see Tables 1-3), and their mean spectral index is −1.34, similar to the value of the rest 45 bright objects −1.38. This implies that the reddening is not strong in faint sources, consistent with the color selection criterion. In contrast, we find that the mean spectral index of the eight FIRST detected quasars −1.07, is evidently redder than that of non-FIRST detections −1.42. This can be likely due to the higher reddening, or the contamination of synchrotron emission in FIRST sources. However, none of these FIRST sources exhibits significant positive correlation between the spectral index and continuum luminosity, indicating that the reddening or synchrotron emission may not be necessarily related with RWB trend.

The anti-correlation of the variability amplitude with rest wavelength has been found in quasars (e.g., Cristiani et al. 1997; Vanden Berk et al. 2004; Zuo et al. 2012). The spectrum shortward of 2500Å shows a steeper slope and is more variable, while the spectrum longward of 2500 Å is flat and less variable relatively for quasars dominated by Balmer emission and Fe II emission lines. This variance mainly comes from the changing of the temperature of the accretion disk (Bian et al. 2012a). It is reasonable to assume that most variability occurs in the inner part of the AGNs, so when the accretion disk becomes hotter, it will produce more high energy photons and the continuum emission peak will move to the short wavelength, which yields a bluer spectra when AGNs become brighter (see Bian et al. 2012a), i.e. the commonly observed BWB trend in AGNs (e.g., Gu & Ai 2011a,b; Zuo et al. 2012). Indeed, we find a BWB trend in half of our sample sources; however, we also find a RWB trend in the remaining half of the sources. In flat-spectrum radio quasars (FSRQs), Gu et al. (2006) proposed that the varying contribution of the thermal emission from the disk relative to the synchrotron jet emission can qualitatively explain the RWB trend. However, this scenario can not be used to explain three quasars with mild RWB correlations (see Section 4.2), because all of them are not detected in FIRST.

It is still unclear what causes the RWB trend in radio-quiet quasars (e.g., Bian et al. 2012a). The line contribution in a broad photometric band could somehow explain the RWB color variability in photometric data (Schmidt et al. 2012; Wilhite et al. 2005); nevertheless, it is hardly applicable to our sample, since the continuum flux in a spectrum that resolves the quasar emission lines and there is no contamination from line emission. Alternatively, the variations of the contri-

bution of the host galaxy could qualitatively produce the RWB trend in multi-epoch spectroscopy with a fixed fiber size (3 arcsec in SDSS-I/II) when seeing varies. The influence of variable seeing conditions on the observed variations has already been noticed in aperture photometry (e.g., Cellone et al. 2000). Since luminous quasars are usually hosted in the bright elliptical galaxies, the host galaxies will be more extended in poor seeing conditions, then their contribution will be relatively smaller within a fixed aperture compared to light from the quasar. This will result in a RWB trend when seeing varies because the host galaxies are usually redder than quasars. We checked the correlations between the spectral index and seeing for three RWB sources with mild correlations. With available seeing, we indeed found correlations at similar confidence level as RWB correlations in two sources, SDSS J030907.49+002419.0 (z = 2.083), and SDSS J031022.10+004130.0 (z = 0.656). Therefore, the effects of host galaxy contribution cannot be completely ruled out, although it is hard to quantitatively evaluate this possibility, and the contribution of host galaxy may not be significant at rest frame wavelength for these two objects.

5.1.1. Comparison with previous works

There have been extensive investigations on the relationship between the spectral shape and continuum variability, especially in radio-loud AGNs (e.g., Fan et al. 1998; Gu & Ai 2011a,b). Two trends of color variations have been found. The BWB trend is commonly found in blazars, as well as in radio quiet AGNs (e.g., Wu et al. 2005; Gu & Ai 2011a,b; Zuo et al. 2012). However, the RWB trend has also been found (e.g., Gu et al. 2006; Bian et al. 2012a), which can be caused by the contribution of thermal emission in case of flat-spectrum radio quasars (Gu et al. 2006). Based on the two-epoch spectroscopy for a sample of quasars, which consists of 312 radio-loud and 232 radio-quiet sources, Bian et al. (2012a) found that half of the objects show the RWB trend, and no obvious difference can be found between sub-samples of radio-quiet and radio-loud quasars. Therefore, our results are consistent with Bian et al. (2012a) in the fact that half of our quasars exhibit a RWB trend, and this RWB trend seems to have no relation with the radio detection. The results will be further investigated in a sample of about 2000 SDSS quasars with pronounced variations from multi-epoch spectroscopy (Guo & Gu 2014, in preparation).

5.2. Line emission

While most sources show positive correlations between the broad line and continuum luminosity, some quasars exhibit anti-correlations, an effect not expected in photoionization model. This anti-correlation could be qualitatively explained by the time delay between the line and continuum variability, because the continuum emission needs a finite amount of time to reach the

broad line region clouds. This is actually why reverberation mapping works for long-term monitoring AGNs (e.g., Kaspi et al. 2000). When we are observing the increased continuum emission, the observed line emission actually happens to correspond to the past declined phase due to the time delay. Therefore, an anti-correlation will be obtained.

5.3. Baldwin effect

Despite the fact that the Baldwin effect has been extensively studied, its origin is still unclear (e.g., Netzer et al. 1992; Dietrich et al. 2002; Baskin & Laor 2004; Wu et al. 2009), and several causes of possible correlations (hence, possible physical causes) have been proposed: correlations with the black hole mass, the Eddington ratio and the luminosity (e.g., Bian & Zhao 2004; Vestergaard & Peterson 2006). Most likely, it could be explained by the trend that more luminous sources have softer Spectral Energy Distribution (Netzer et al. 1992; Dietrich et al. 2002), which produce less ionizing photons.

While the Baldwin effect has been studied extensively for AGN samples (e.g., Bian et al. 2012b), few works have been done on the Baldwin effect in individual sources. With multi-epoch spectroscopy, we investigate the Baldwin effect for our sample objects. As described in Section 4, most sources exhibit an anti-correlation between EW and continuum luminosity, as expected from Baldwin effect, although the correlations are usually weak. As claimed in Wilhite et al. (2005) the broad lines are less variable than the underlying continuum, resulting in a relationship known as the intrinsic Baldwin effect, which is intrinsic to each object (Kinney et al. 1990). However, the intrinsic Baldwin effect in each object will be altered by the light-travel time effects in the broad-line region. Indeed, it has been shown that the scatter in the continuum-emission-line correlations is greatly reduced by removing light-travel time effects so that the emission-line flux are referred to the continuum that is driving them (e.g., Pogge & Peterson 1992). Unfortunately, we are unable to remove the light-travel time effects for our quasars due to the limited spectroscopic data. Interestingly, we also found a strong positive correlation between the EW and continuum luminosity (i.e. negative Baldwin effect) in SDSS J030639.57+000343.1 (broad Hα, see Fig. 7) at $\sim$ 99% confidence level. This however is most likely caused by increasing host contamination toward fainter luminosities (see Shen et al. 2011).

5.3.1. Comparison with previous works

As shown in Fig. 8, a strong anti-correlation has been found for the Mg II line when all the measurements from multi-epoch spectra are put together, suggesting a Baldwin effect for the

whole sample. However, some scatters are also found, which is likely, at least partly, caused by the mixture of the intrinsic Baldwin effect and light-travel time effects in each object. The Baldwin effect in Mg II line is consistent with previous works. In the comprehensive study for DR7 quasar catalog (105,783 quasars), the strong Baldwin effects were found in both Mg II and C IV (Shen et al. 2011). In contrast, the Baldwin effect in Hβ is still unclear. The weak negative Baldwin effect was found for Hβ in the forms of $EW \propto L^{0.2}$, and $EW \propto L^{0.1}$ from $\sim$ 22,000 quasars in 2dF+6dF surveys (Croom et al. 2002), and $\sim$ 40,000 SDSS quasars (Greene & Ho 2005; Netzer & Trakhtenbrot 2007), respectively. It was suggested that this unexpected effect is likely caused by the luminosity-dependent change in the ratio of disc to non-disc continuum components (Croom et al. 2002). Indeed, although our sample is rather small compared to their samples, we found a strong negative Baldwin effect in Hβ $EW \propto L^{0.14}$ with a Spearman correlation coefficient r_s = 0.5 at $\gg$ 99.9% confidence level, consistent with their results. The negative Baldwin effect between the broad Hβ EW and L_{5100} has also been found below $L_{5100} \sim 10^{45}$erg s^{-1} in DR7 quasars (see their Fig. 12, Shen et al. 2011). However, the authors argued that it can be most likely due to the contamination from the host galaxy. When we restrict $L_{5100} \geq 10^{45}$erg s^{-1}, we did not find pronounced Baldwin effect in Hβ for our sample. However, the small sample size with only 13 quasars at $L_{5100} \geq 10^{45}$erg s^{-1} precludes us to draw firm conclusions. Similarly, we failed to find Baldwin effect in C IV , which may be caused by the narrow L_{1350} coverage (Shields 2007) (see Fig. 8).

5.4. Line width

An anti-correlation between the FWHM and luminosity of emission lines has been found in previous works (e.g., Wills et al. 1993). An intermediate-line region (ILR) is hypothesized to explain the anti-correlation, which is located between the narrow-line region and the very broad-line region, i.e., there are two distinct portions of the broad-line region. In the empirical relation of black hole mass estimations (e.g., Kaspi et al. 2000), the black hole mass can be obtained from

$$M_{\rm BH} \propto V^2 \times R_{\rm BLR} \propto {\rm FWHM}^2 \times L^{\beta}, \quad (3)$$

where the $M_{\rm BH}$ is the black hole mass, V is velocity of the BLR gas clouds, $R_{\rm BLR}$ is BLR radius, β is the index of the empirical $R_{\rm BLR}$ - L relation, and L is either the continuum or emission line luminosity (e.g., Wu et al. 2004). Therefore, an anti-correlation between emission line luminosity and the line width would be expected in individual sources, which indeed has been found in some quasars. However, we find positive correlations between FWHM and line luminosity in most sources (see Tables 1 - 3). The positive correlations become even more evident when putting all quasars together in Fig. 10, which is consistent with Wilhite et al. (2005). This result can be explained with two components in BLR, with the broad line base (the inner BLR) more variable

than the line core, which is expected because with the radius increasing, the characteristics of the variation will be diluted and the reprocessing of the seed photons will consume the energy of the variability (see Wilhite et al. 2005). In the double-peaked broad Hα source 3C 390.3, Zhang (2013) argued that this unexpected positive correlation can be naturally explained, due to the different time delays for different parts of the disk-like BLRs in one short period with the theoretical accretion disk model.

6. Conclusions

We have investigated the optical variability at various aspects for a sample of 60 SDSS quasars with at least six-epoch spectroscopic observations. The main results are summarized as follows:

(1) We verify the strong anti-correlation between the variability and continuum luminosity, consistent with previous works. A mild anti-correlation is discovered between variability and redshift. However, we find no significant correlations between the variability and black hole mass or Eddington ratio. In individual sources, half of the sample objects show BWB, while the rest half exhibit RWB. Although the mechanism of RWB is unclear, the effects of host galaxy contribution due to seeing variations can not be completely ruled out.

(2) As expected from photoionization model, the positive correlations between the broad emission line and continuum luminosity are found in most individual sources, as well as for the whole sample. We confirm the Baldwin effect in most individual objects and the whole sample, while the negative Baldwin effect were also found in several quasars, which can be at least partly (if not all) due to the host galaxy contamination.

(3) We find positive correlations between the broad emission line luminosity and line width in most individual quasars, as well as the whole sample, implying a more variable line base than the line core.

We thank Zhaoyu Chen for help with data reduction. HXG thanks the Center for Astrophysics of USTC for teaching during his stay in USTC. This work is supported by the National Science Foundation of China (grant 11373056) and by the Science and Technology Commission of Shanghai Municipality (14ZR1447100).

Funding for SDSS-III has been provided by the Alfred P. Sloan Foundation, the Participating Institutions, the National Science Foundation, and the U.S. Department of Energy Office of Science. The SDSS-III web site is http://www.sdss3.org.

SDSS-III is managed by the Astrophysical Research Consortium for the Participating Institutions of the SDSS-III Collaboration including the University of Arizona, the Brazilian Participation Group, Brookhaven National Laboratory, University of Cambridge, Carnegie Mellon University, University of Florida, the French Participation Group, the German Participation Group, Harvard University, the Instituto de Astrofisica de Canarias, the Michigan State/Notre Dame/JINA Participation Group, Johns Hopkins University, Lawrence Berkeley National Laboratory, Max Planck Institute for Astrophysics, Max Planck Institute for Extraterrestrial Physics, New Mexico State University, New York University, Ohio State University, Pennsylvania State University, University of Portsmouth, Princeton University, the Spanish Participation Group, University of Tokyo, University of Utah, Vanderbilt University, University of Virginia, University of Washington, and Yale University.

REFERENCES

Abazajian, K. N., Adelman-McCarthy, J. K., Agüeros, M. A., et al. 2009, ApJS, 182, 543

Ahn, C. P., Alexandroff, R., Allende Prieto, C., et al. 2012, ApJS, 203, 21

Ai, Y. L., Yuan, W., Zhou, H. Y., et al. 2010, ApJ, 716, L31

Angione, R. J., & Smith, H. J. 1972, External Galaxies and Quasi-Stellar Objects, 44, 171

Baldwin, J. A. 1977, Lick Observatory Bulletin, 748, 1

Baskin, A., & Laor, A. 2004, MNRAS, 350, L31

Becker, R. H., White, R. L., & Helfand, D. J. 1995, ApJ, 450, 559

Bian, W., & Zhao, Y. 2004, MNRAS, 347, 607

Bian, W.-H., Zhang, L., Green, R., & Hu, C. 2012a, ApJ, 759, 88

Bian, W.-H., Fang, L.-L., Huang, K.-L., & Wang, J.-M. 2012b, MNRAS, 427, 2881

Cellone, S. A., Romero, G. E., & Combi, J. A. 2000, AJ, 119, 1534

Chen, Z., Gu, M., & Cao, X. 2009, MNRAS, 397, 1713

Cid Fernandes, R., Jr., Aretxaga, I., & Terlevich, R. 1996, MNRAS, 282, 1191

Cid Fernandes, R., Sodré, L., Jr., & Vieira da Silva, L., Jr. 2000, ApJ, 544, 123

Cristiani, S., Trentini, S., La Franca, F., & Andreani, P. 1997, A&A, 321, 123

Cristiani, S., Trentini, S., La Franca, F., et al. 1996, A&A, 306, 395

Croom, S. M., Rhook, K., Corbett, E. A., et al. 2002, MNRAS, 337, 275

Dawson, K. S., Schlegel, D. J., Ahn, C. P., et al. 2013, AJ, 145, 10

Dietrich, M., Hamann, F., Shields, J. C., et al. 2002, ApJ, 581, 912

Fan, J. H., Xie, G. Z., Lin, R. G., & Qin, Y. P. 1998, A&AS, 133, 217

Greene, J. E., & Ho, L. C. 2005, ApJ, 630, 122

Gu, M. F., Lee, C.-U., Pak, S., Yim, H. S., & Fletcher, A. B. 2006, A&A, 450, 39

Gu, M.-F., & Ai, Y. L. 2011a, A&A, 528, A95

Gu, M. F., & Ai, Y. L. 2011b, A&A, 534, A59

Gu, M. F., & Li, S.-L. 2013, A&A, 554, A51

Guo, H., & Gu, M. 2014, Journal of Astrophysics and Astronomy, in press (arXiv:1306.0273)

Hook, I. M., McMahon, R. G., Boyle, B. J., & Irwin, M. J. 1994, MNRAS, 268, 305

Kaspi, S., Smith, P. S., Netzer, H., et al. 2000, ApJ, 533, 631

Kinney, A. L., Bohlin, R. C., Blades, J. C., & York, D. G. 1990, ESA Special Publication, 310, 517

Li, S.-L., & Cao, X. 2008, MNRAS, 387, L41

Netzer, H., Laor, A., & Gondhalekar, P. M. 1992, MNRAS, 254, 15

Netzer, H., & Trakhtenbrot, B. 2007, ApJ, 654, 754

Pogge, R. W., & Peterson, B. M. 1992, AJ, 103, 1084

Richards, G. T., Fan, X., Newberg, H. J., et al. 2002, AJ, 123, 2945

Sakata, Y., Morokuma, T., Minezaki, T., et al. 2011, ApJ, 731, 50

Schlegel, D. J., Finkbeiner, D. P., & Davis, M. 1998, ApJ, 500, 525

Schmidt, K. B., Rix, H.-W., Shields, J. C., et al. 2012, ApJ, 744, 147

Schneider, D. P., Richards, G. T., Hall, P. B., et al. 2010, AJ, 139, 2360

Shen, Y., Richards, G. T., Strauss, M. A., et al. 2011, ApJS, 194, 45

Shields, J. C. 2007, The Central Engine of Active Galactic Nuclei, 373, 355 Tenorio-Tagle, G., Franco, J., & Melnick, J. 1992, MNRAS, 255, 713

Trevese, D., Kron, R. G., Majewski, S. R., Bershady, M. A., & Koo, D. C. 1994, ApJ, 433, 494

Ulrich, M.-H., Maraschi, L., & Urry, C. M. 1997, ARA&A, 35, 445

Vanden Berk, D. E., Richards, G. T., Bauer, A., et al. 2001, AJ, 122, 549

Vanden Berk, D. E., Wilhite, B. C., Kron, R. G., et al. 2004, ApJ, 601, 692

Véron-Cetty, M.-P., Joly, M., & Véron, P. 2004, A&A, 417, 515

Vestergaard, M., & Wilkes, B. J. 2001, ApJS, 134, 1

Vestergaard, M., & Peterson, B. M. 2006, ApJ, 641, 689

Wilhite, B. C., Vanden Berk, D. E., Kron, R. G., et al. 2005, ApJ, 633, 638

Wilhite, B. C., Brunner, R. J., Grier, C. J., Schneider, D. P., & vanden Berk, D. E. 2008, MNRAS, 383, 1232

Wills, B. J., Brotherton, M. S., Fang, D., Steidel, C. C., & Sargent, W. L. W. 1993, ApJ, 415, 563

Wold, M., Brotherton, M. S., & Shang, Z. 2007, MNRAS, 375, 989

Wold, M., Brotherton, M. S., & Shang, Z. 2008, American Institute of Physics Conference Series, 1053, 55

Wu, J., Vanden Berk, D. E., Brandt, W. N., et al. 2009, ApJ, 702, 767

Wu, J., Zhou, X., Peng, B., et al. 2005, MNRAS, 361, 155

Wu, X.-B., Wang, R., Kong, M. Z., Liu, F. K., & Han, J. L. 2004, A&A, 424, 793

Yee, H. K. C. 1980, ApJ, 241, 894

Zhang, K., Wang, T.-G., Yan, L., & Dong, X.-B. 2013, ApJ, 768, 22

Zhang, X.-G. 2013, MNRAS, 429, 2274

Zuo, W., Wu, X.-B., Liu, Y.-Q., & Jiao, C.-L. 2012, ApJ, 758, 104

This preprint was prepared with the AAS LaTeX macros v5.2.

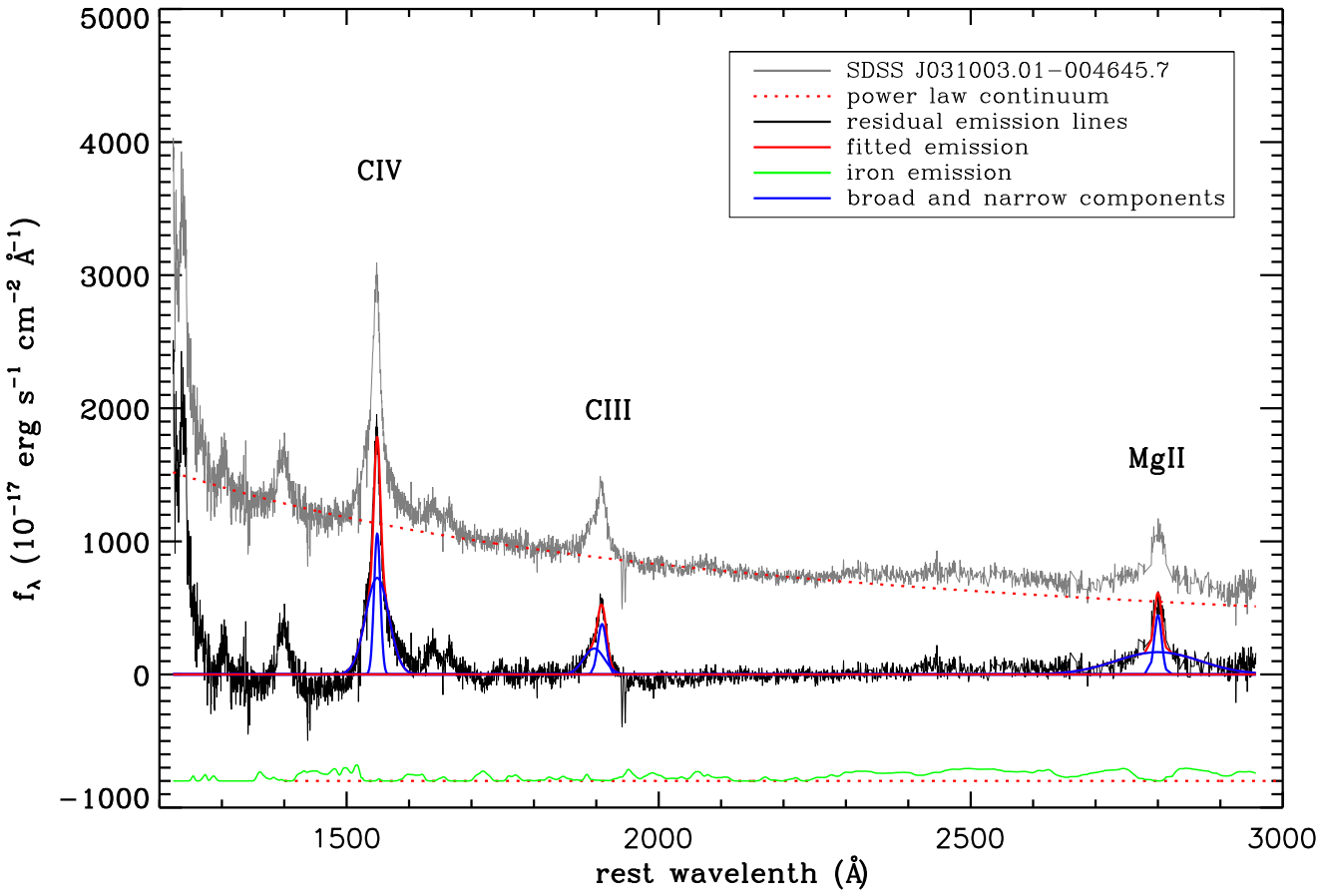


Fig. 1.— The spectral analysis of SDSS J031003.01-004645.7 as an example. The grey and black lines are the original and continuum-subtracted spectrum, respectively. The red dotted line represents the power-law continuum. The blue lines are each Gaussian component of various emission lines, and the red solid line is the integrated profile. The green line is Fe II emission, which is shifted downwards with arbitrary unit for the sake of presentation. The prominent emission lines, C IV , C III , and Mg II are marked.

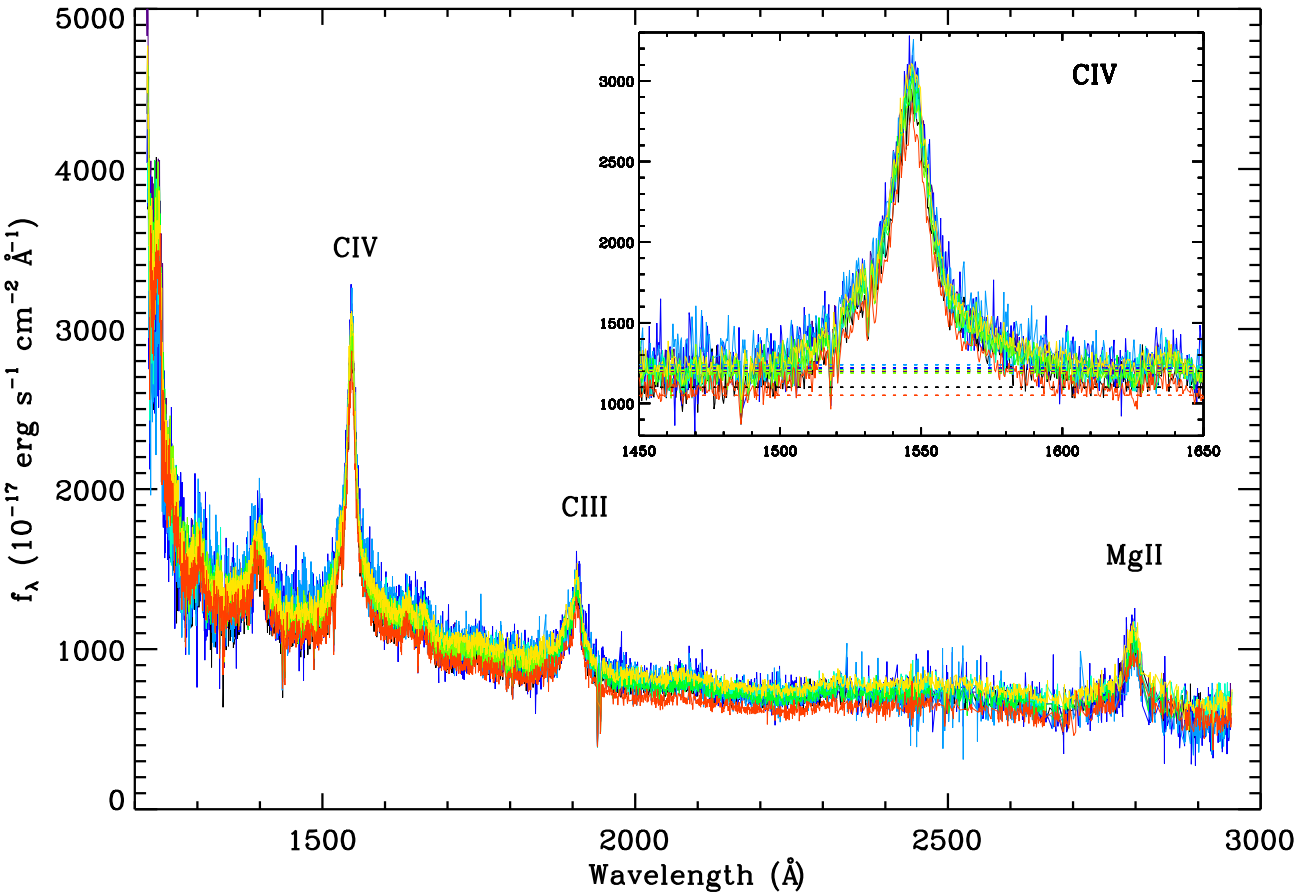


Fig. 2.— The nine-epoch SDSS spectra of SDSS J031003.01-004645.7 (z = 2.115) in the rest frame. Each epoch is indicated with different color. The dashed lines in the inset are the local continuum for C IV .

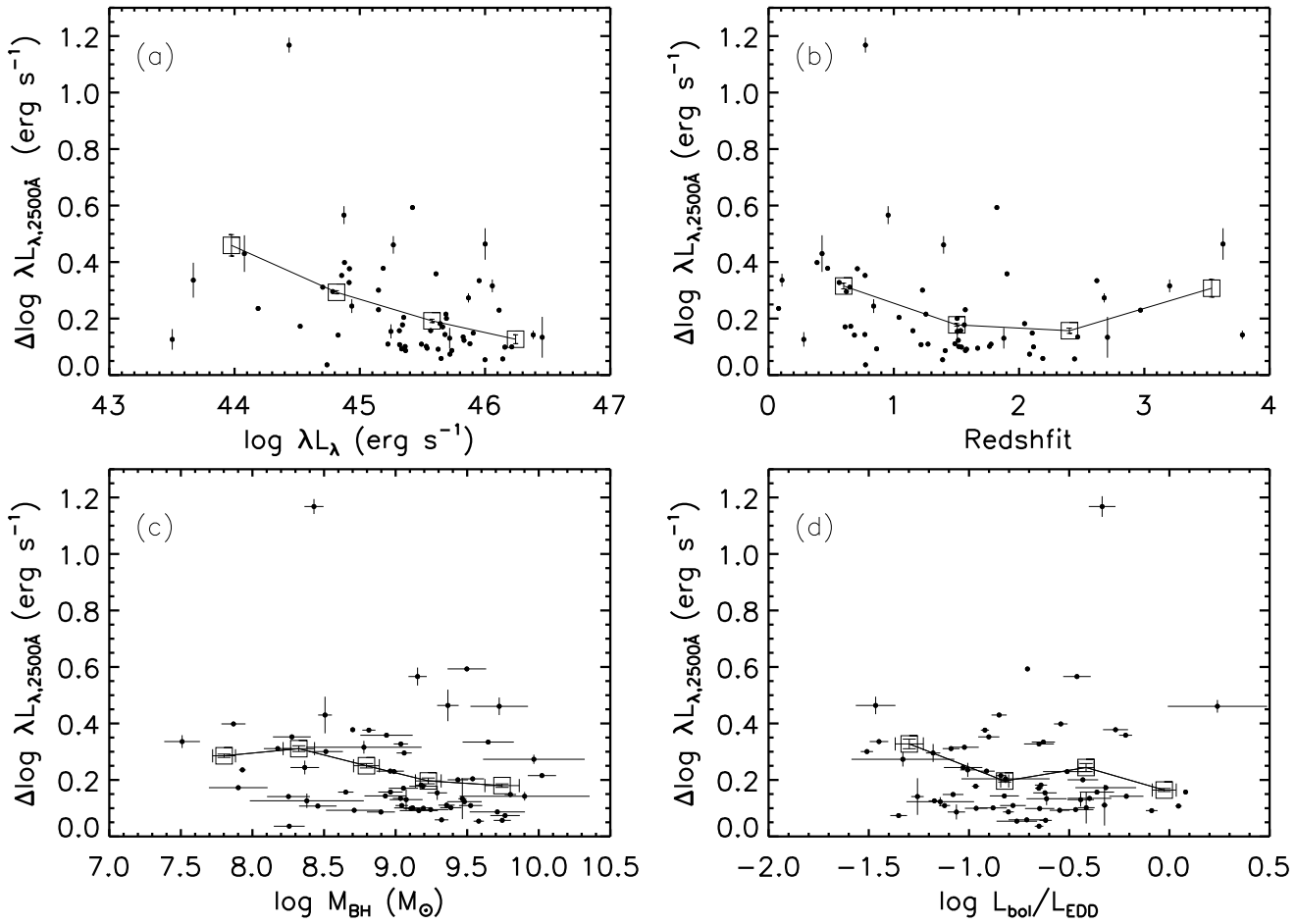


Fig. 3.— (a): The variability amplitude versus continuum luminosity at 2500Å. The continuum luminosity is the multi-epoch averaged value; (b): The variability amplitude versus redshift; (c): The variability amplitude versus black hole masses; (d): The variability amplitude versus Eddington ratio. In each panel, the squares represent the mean variability amplitude in bins of *x*-axis parameters. The different bins are divided by (a) 44.5, 45, 46; (b) 1, 2, 3; (c) 8.0, 8.5, 9.0, 9.5; (d) -1.1, -0.6, -0.2.

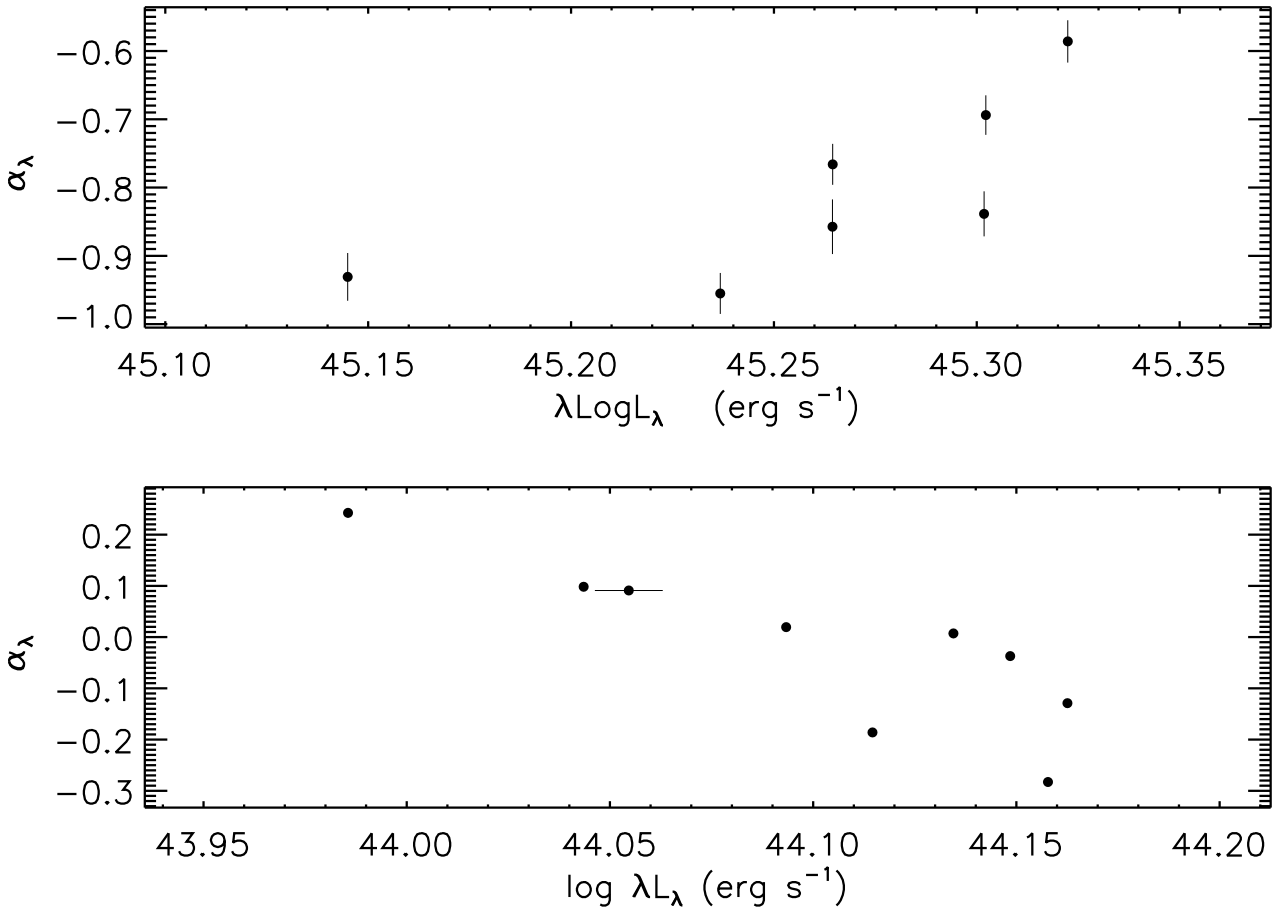


Fig. 4.— The examples of correlations between the spectral index and the continuum luminosity at 2500 Å: RWB (SDSS J031022.10+004130.0, top), and BWB (SDSS J30639.57+000343.1, bottom). The errors of the spectral index and continuum luminosity are indicated by the vertical and horizontal lines, respectively, which are not evident when less than the symbol size.

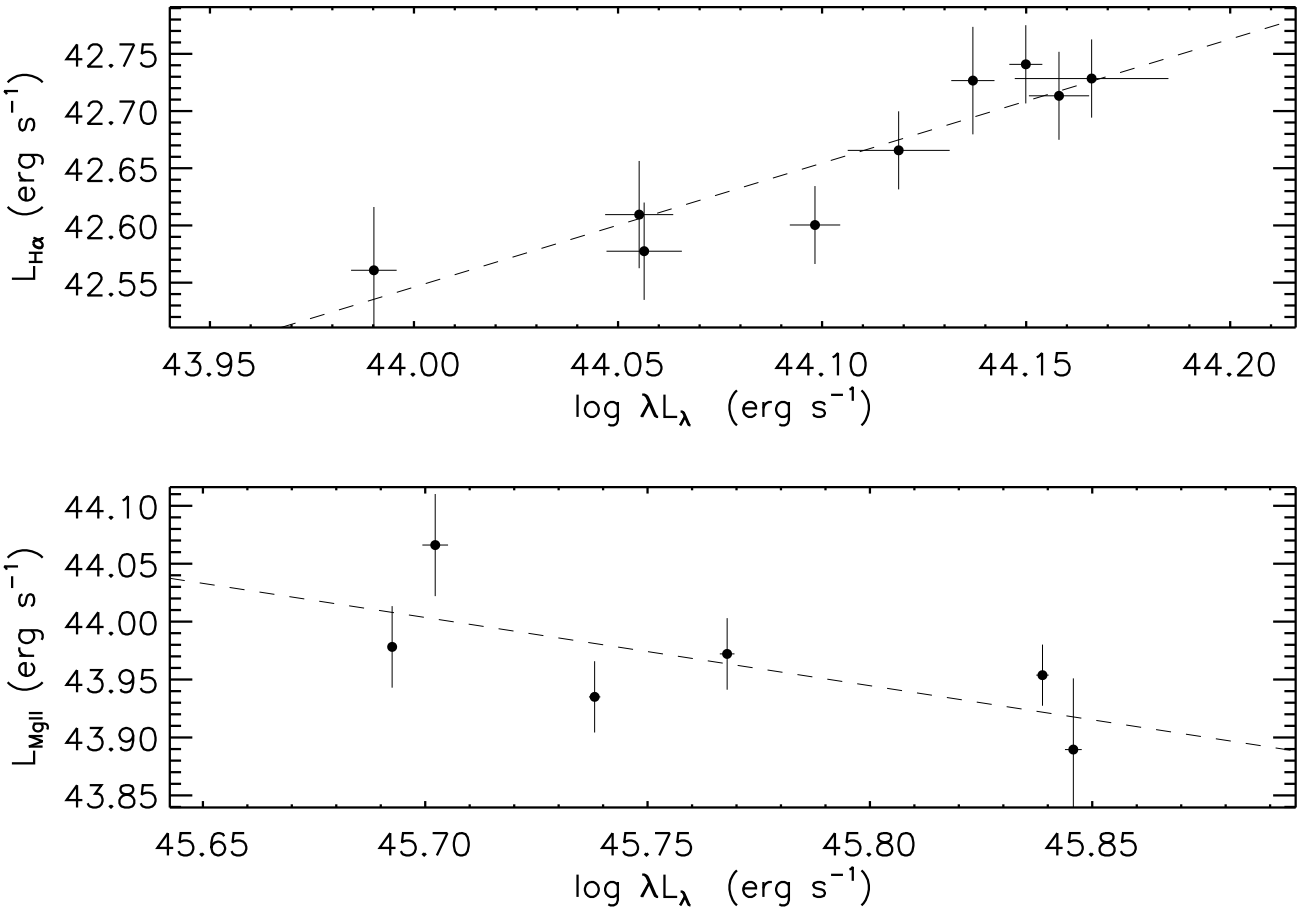


Fig. 5.— The examples of the positive correlation (SDSS J030639.57-000343.1, for Hα , top) and anti-correlation (SDSS J021754.80+000234.0, for Mg II , bottom) between the broad emission line and continuum luminosity. The dashed lines are linear fits (see text for details). The errors of the broad emission line and continuum luminosity are indicated by the vertical and horizontal lines, respectively, which are not evident when less than the symbol size.

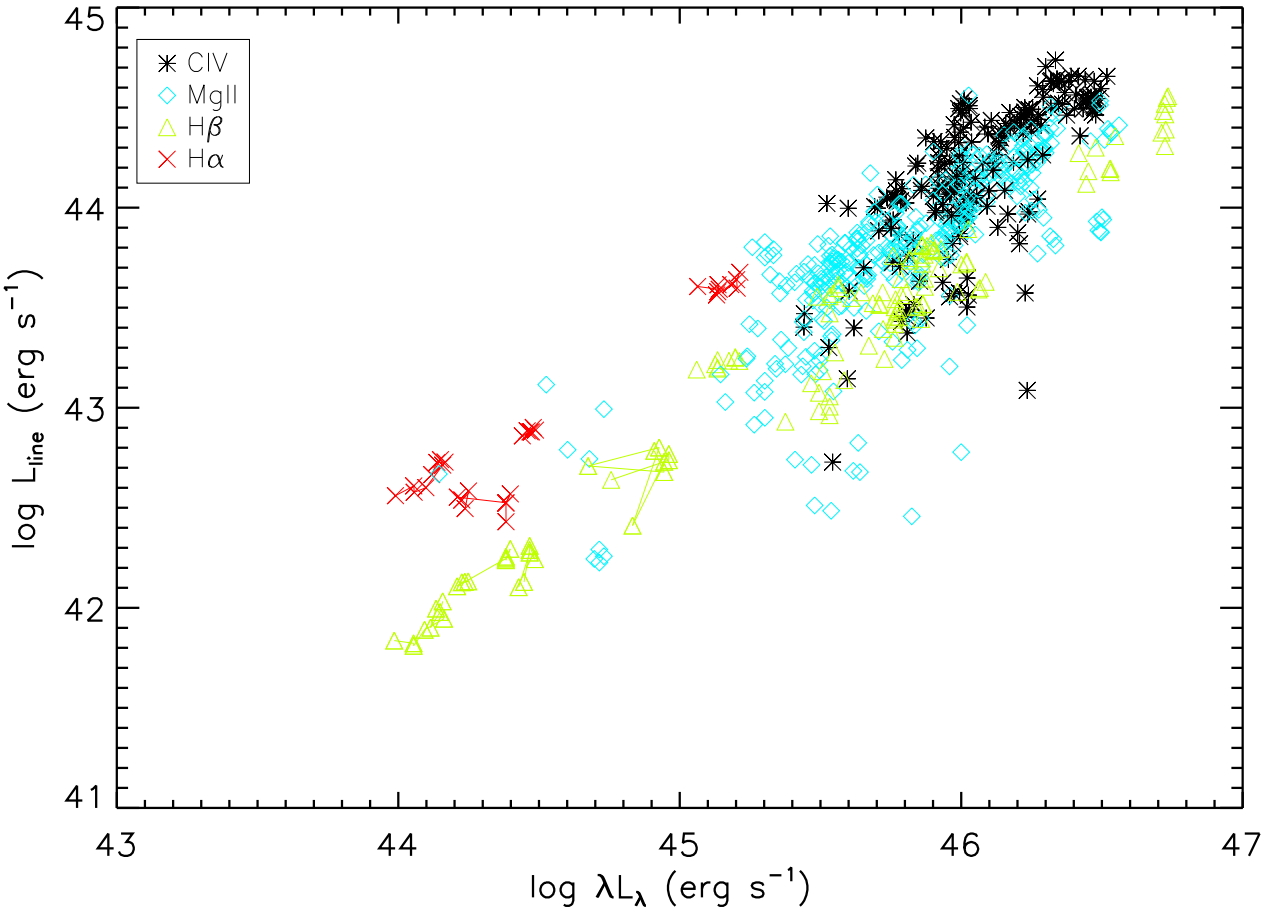


Fig. 6.— The broad emission line and continuum luminosity from all multi-epoch spectra of our sample. The continuum luminosity for broad C IV , Mg II , Hβ , and Hα are at 1350Å, 3000Å, 5100Å, and 5100Å, respectively. The measurements from multi-epoch spectra for the same object are connected with solid lines for Hα in four sources, and Hβ in four sources.

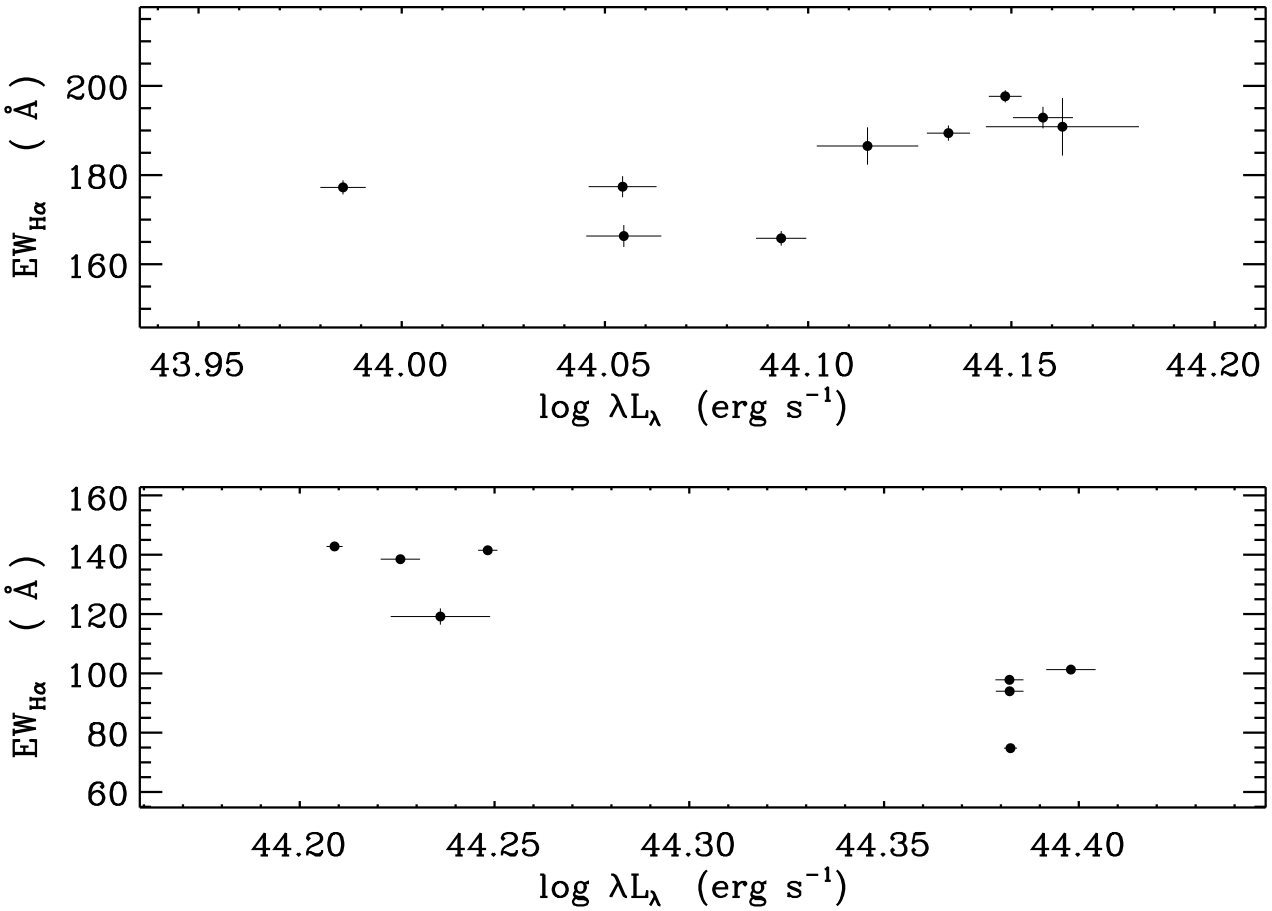


Fig. 7.— The examples of the positive correlation (SDSS J030639.57+000343.1, for Hα , top) and negative correlation (SDSS J031027.82-004950.7, for Hα , bottom) between the broad line equivalent width and continuum luminosity. The errors of the EW and continuum luminosity are indicated by the vertical and horizontal lines, respectively, which are not evident when less than the symbol size.

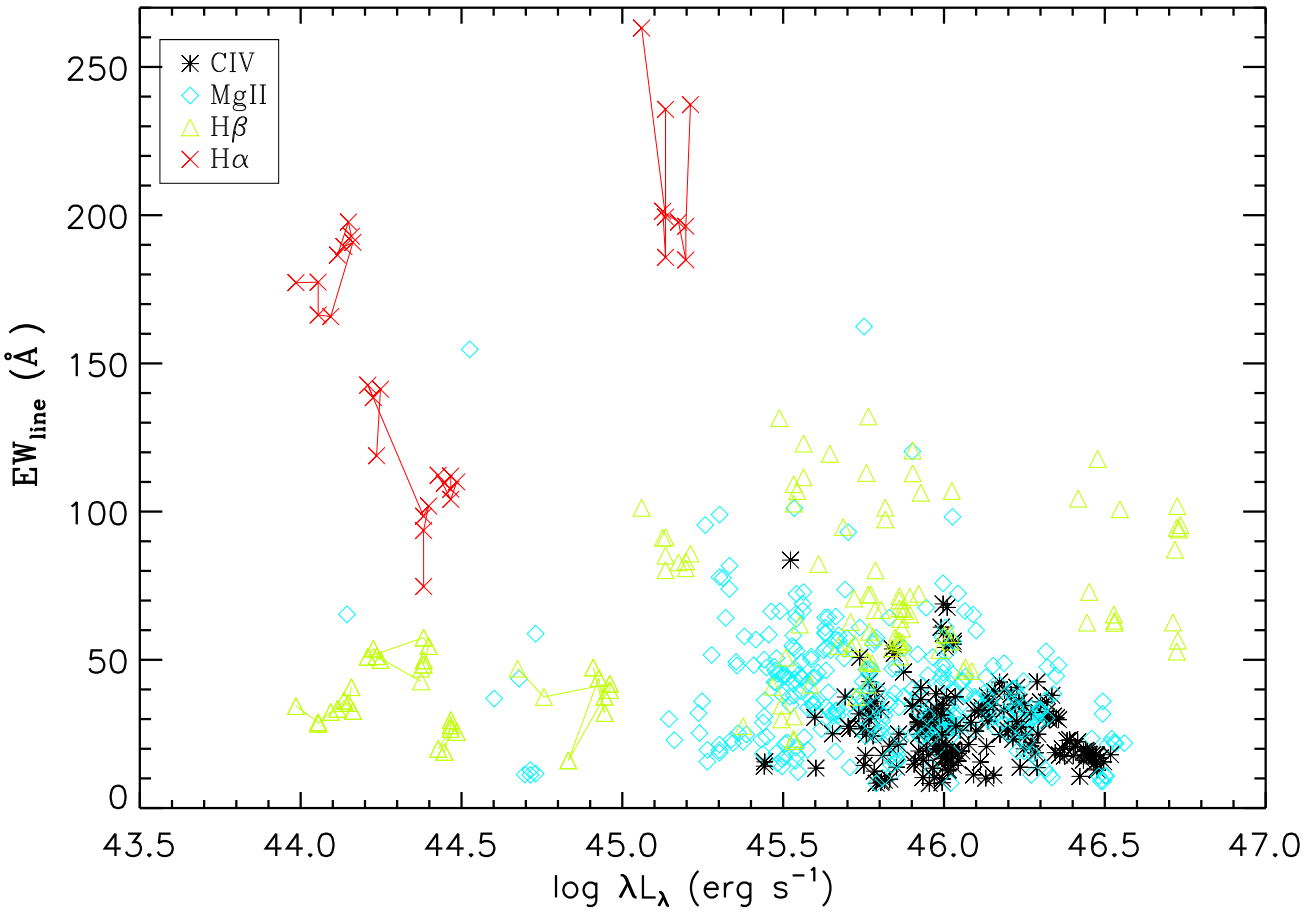


Fig. 8.— The broad emission line equivalent width and continuum luminosity from all multi-epoch spectra of our sample. The measurements from multi-epoch spectra for the same object are connected with solid lines for Hα in four sources, and Hβ in four sources.

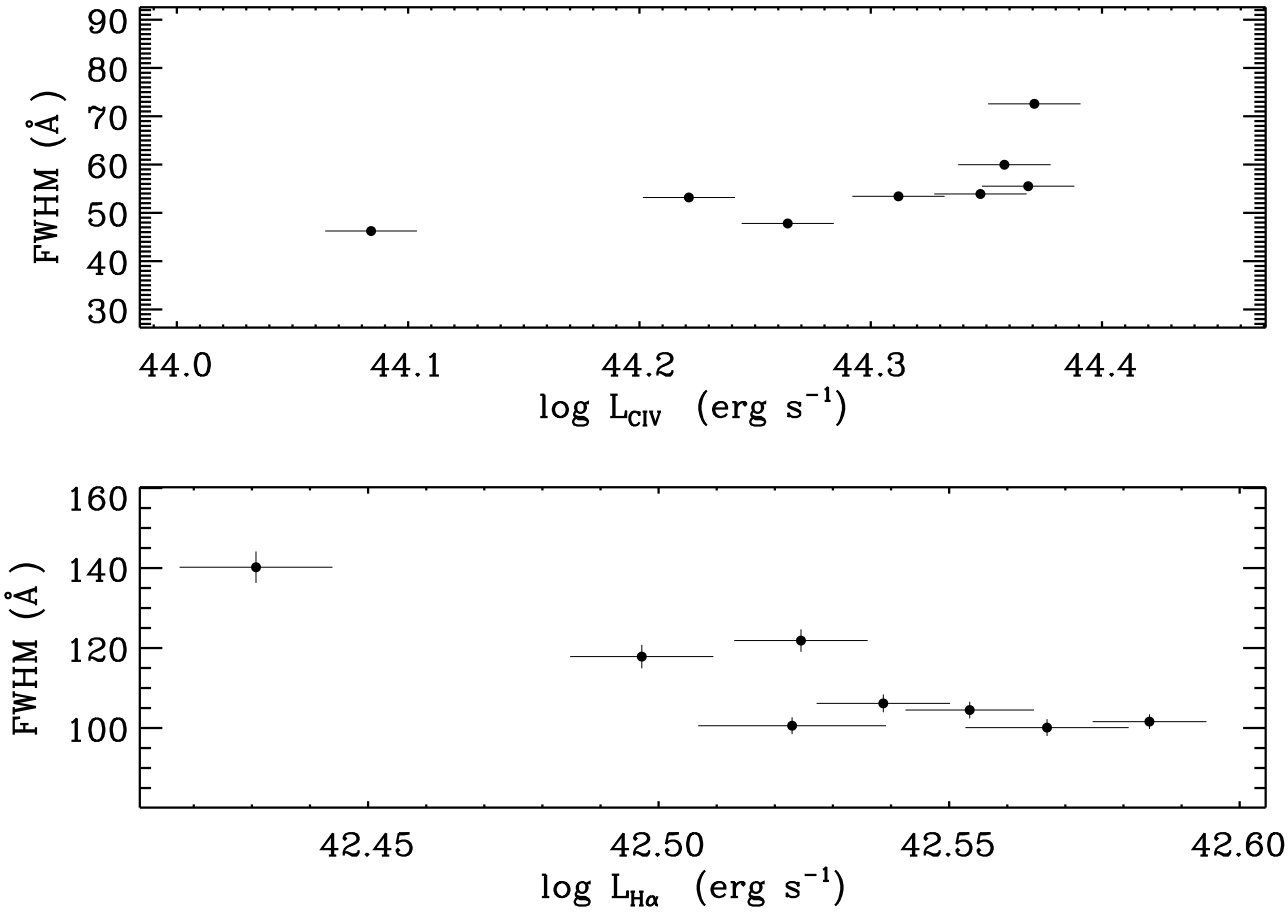


Fig. 9.— The examples of the positive correlation (SDSS J031131.41-002127.4, for C IV , top) and negative correlation (SDSS J031027.82-004950.7, for Hα , bottom) between the FWHM and luminosity of broad lines. The errors of the FWHM and line luminosity are indicated by the vertical and horizontal lines, respectively, which are not evident when less than the symbol size.

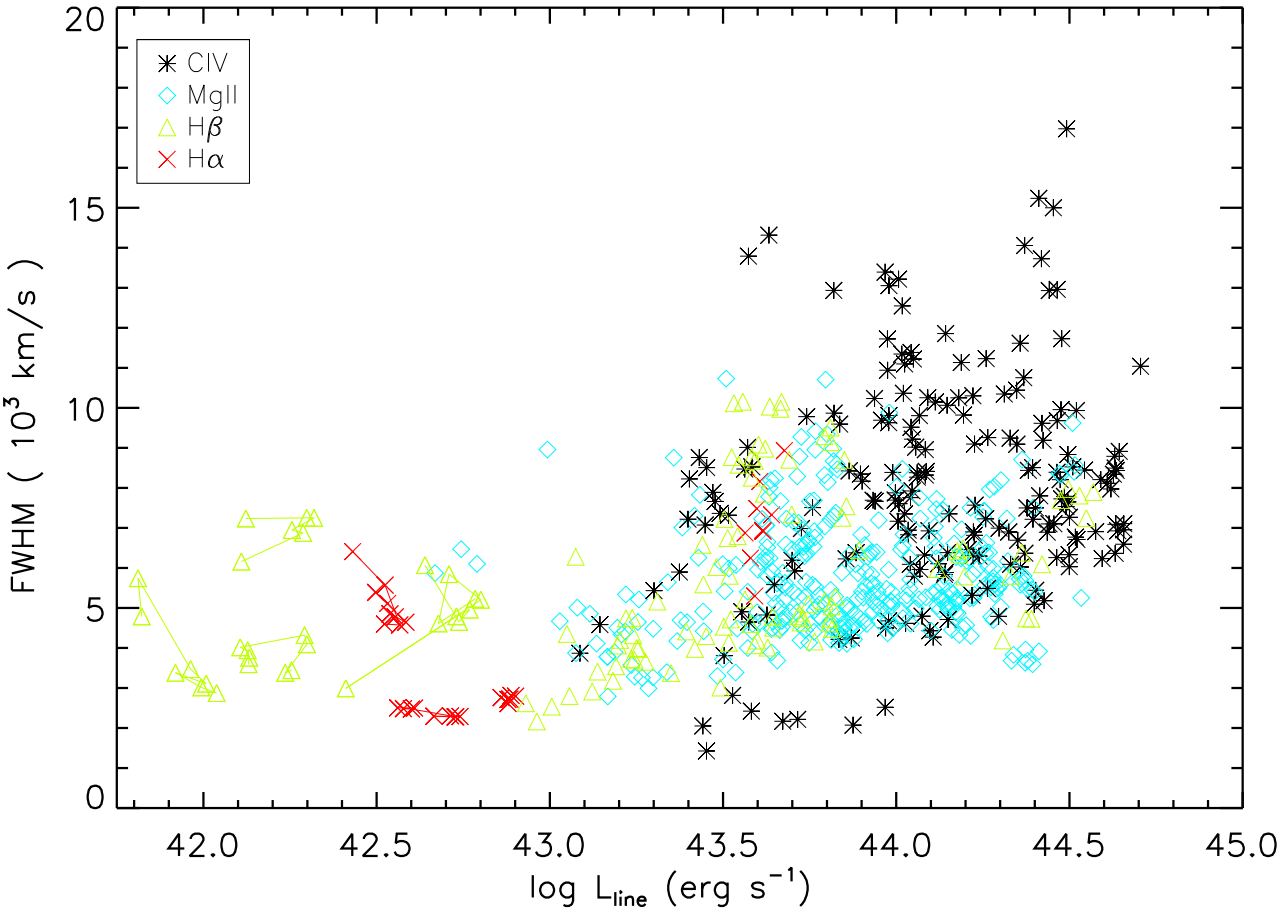


Fig. 10.— The broad emission line FWHM and line luminosity from all multi-epoch spectra of our sample. The measurements from multi-epoch spectra for the same object are connected with solid lines for Hα in three sources, and Hβ in four sources.

Table 1. Quasars at $z \leq 0.4$

Object (SDSS J)	z	i	N	log $M_{\rm bh}$	$\dot{m}$	R	$L_{\rm con}$ - α_λ		$L_{\rm con}$ - $L_{\rm H\beta}$		$L_{\rm con}$ - $L_{\rm H\alpha}$		$L_{\rm con}$ - $EW_{\rm H\beta}$		$L_{\rm con}$ - $EW_{\rm H\alpha}$		$L_{\rm H\beta}$ - FWHM		$L_{\rm H\alpha}$ - FWHM	
		(mag)		($M_\odot$)			r	p	r	p	r	p	r	p	r	p	r	p	r	p
(1)	(2)	(3)	(4)	(5)	(6)	(7)	(8)	(9)	(10)	(11)	(12)	(13)	(14)	(15)	(16)	(17)	(18)	(19)	(20)	(21)
030639.57+000343.1	0.107	16.83	9	7.50	0.24	5.3	-0.89	5E-4	0.86	1E-3	0.86	2E-3	0.50	0.17	0.78	0.01	-0.32	0.35	-0.35	0.31
031027.82-004950.7	0.081	15.63	8	7.92	0.10	-	-0.59	0.11	0.92	8E-4	-0.14	0.73	-0.07	0.86	-0.78	0.02	0.19	0.65	-0.66	0.07
031142.02-005918.9	0.281	18.69	6	8.37	0.04	-	0.37	0.46	0.60	0.20	0.71	0.11	0.54	0.26	-0.48	0.32	0.75	0.08	0.54	0.26
031427.45-011152.3	0.387	18.33	8	7.86	0.53	-	-0.16	0.66	0.73	0.02	0.63	0.06	-0.51	0.15	-0.46	0.21	0.13	0.73	0.66	0.04

Note. — The quasars at $z \leq 0.4$ in our sample: Col. (1) object name; Col. (2) redshift; Col. (3) i-band apparent magnitude; Col. (4) number of spectroscopic observations; Col. (5) black hole mass; Col. (6) Eddington ratio, defined as $L_{\rm bol}/L_{\rm Edd}$; Col. (7) radio loudness, $R = f_{\rm 6cm}/f_{2500}$; Cols. (8) - (21) the Spearman rank correlation coefficients and probability level for $L_{\rm con}$ - α_λ, $L_{\rm con}$ - $L_{\rm H\beta}$, $L_{\rm con}$ - $L_{\rm H\alpha}$, $L_{\rm con}$ - $EW_{\rm H\beta}$, $L_{\rm con}$ - $EW_{\rm H\alpha}$, $L_{\rm H\beta}$ - FWHM, and $L_{\rm H\alpha}$ - FWHM.

Table 2. Quasars at $0.4 < z \leq 0.8$

Object (SDSS J)	z	i	N	log $M_{\rm bh}$	$\dot{m}$	R	$L_{\rm con}$ - α_λ		$L_{\rm con}$ - $L_{\rm MgII}$		$L_{\rm con}$ - $L_{\rm H\beta}$		$L_{\rm con}$ - $EW_{\rm MgII}$		$L_{\rm con}$ - $EW_{\rm H\beta}$		$L_{\rm MgII}$ - FWHM		$L_{\rm H\beta}$ - FWHM	
		(mag)		($M_\odot$)			r	p	r	p	r	p	r	p	r	p	r	p	r	p
(1)	(2)	(3)	(4)	(5)	(6)	(7)	(8)	(9)	(10)	(11)	(12)	(13)	(14)	(15)	(16)	(17)	(18)	(19)	(20)	(21)
021953.04-004434.2	0.686	19.60	6	8.25	-0.76	-	-0.08	0.87	0.43	0.39	0.20	0.70	-0.54	0.27	-0.02	0.95	0.02	0.96	0.60	0.20
022214.38-001745.3	0.773	21.18	6	8.42	-1.06	-	-0.60	0.28	0.89	0.03	0.80	0.10	-0.70	0.19	0.50	0.39	-0.20	0.74	0.40	0.50
022331.90-001605.5	0.771	19.00	6	8.27	-0.46	-	0.09	0.87	-0.10	0.87	0.99	1E-4	-0.90	0.03	-0.90	0.03	0.70	0.18	-0.50	0.40
022335.84+002351.8	0.774	19.07	9	8.25	-0.64	-	-0.11	0.76	-0.08	0.83	0.25	0.52	-0.08	0.83	-0.07	0.86	-0.51	0.15	0.11	0.76
022556.34+001345.3	0.709	19.51	7	8.81	-1.12	-	0.46	0.29	0.78	0.04	0.82	0.02	-0.03	0.93	-0.11	0.82	0.82	0.02	0.57	0.18
030458.96+000235.7	0.564	18.36	10	9.03	-1.17	404.4	-0.76	9E-3	0.01	0.98	0.08	0.83	-0.50	0.13	-0.43	0.21	0.83	3E-3	0.72	0.01
030745.95+000833.4	0.427	19.02	9	8.50	0.05	-	-0.59	0.11	-0.26	0.53	0.26	0.50	-0.45	0.26	-0.26	0.53	0.90	2E-3	0.59	0.11
030911.64+002358.8	0.611	17.22	10	9.05	-0.62	-	-0.66	0.07	0.38	0.35	0.26	0.53	-0.69	0.05	-0.21	0.61	0.97	4E-5	-0.17	0.69
030939.45-000339.2	0.769	17.11	8	8.92	-0.36	-	0.16	0.69	-0.02	0.95	0.54	0.16	-0.19	0.65	0.33	0.41	-0.88	3E-3	0.73	0.03
031022.10+004130.0	0.656	19.47	7	7.90	-0.31	-	0.67	0.09	-0.46	0.29	0.18	0.70	-0.42	0.33	-0.32	0.48	0.96	1E-4	0.71	0.01
031226.12-003708.9	0.621	18.98	10	9.06	-1.51	1227.7	-0.06	0.86	0.28	0.46	0.92	5E-4	-0.87	2E-3	-0.47	0.20	-0.16	0.66	-0.06	0.86
032142.83-003225.7	0.648	19.14	6	8.17	-0.46	-	0.30	0.62	0.00	1.00	0.99	1E-4	-0.70	0.18	-0.10	0.87	0.69	0.18	-0.10	0.87
032205.04+001201.4	0.471	17.48	6	8.70	-0.71	-	-0.71	0.11	0.42	0.39	0.94	4E-3	-0.37	0.46	0.09	0.87	0.25	0.62	0.37	0.46

Note. — The quasars at $0.4 < z \leq 0.8$ in our sample: Col. (1) object name; Col. (2) redshift; Col. (3) i-band apparent magnitude; Col. (4) number of spectroscopic observations; Col. (5) black hole mass; Col. (6) Eddington ratio, defined as $L_{\rm bol}/L_{\rm Edd}$; Col. (7) radio loudness, $R = f_{\rm 6cm}/f_{2500}$; Cols. (8) - (21) the Spearman rank correlation coefficients and probability level for $L_{\rm con}$ - α_λ, $L_{\rm con}$ - $L_{\rm MgII}$, $L_{\rm con}$ - $L_{\rm H\beta}$, $L_{\rm con}$ - $EW_{\rm MgII}$, $L_{\rm con}$ - $EW_{\rm H\beta}$, $L_{\rm MgII}$ - FWHM, and $L_{\rm H\beta}$ - FWHM.

Table 3. Quasars at $z > 0.8$

Object (SDSS J)	z	i	N	log M_{bh}	$\dot{m}$	R	L_{con} - α_λ		L_{con} - $L_{C_{IV}}$		L_{con} - L_{MgII}		L_{con} - $EW_{C_{IV}}$		L_{con} - EW_{MgII}		$L_{C_{IV}}$ - FWHM		L_{MgII} - FWHM	
		(mag)		($M_\odot$)			r	p	r	p	r	p	r	p	r	p	r	p	r	p
(1)	(2)	(3)	(4)	(5)	(6)	(7)	(8)	(9)	(10)	(11)	(12)	(13)	(14)	(15)	(16)	(17)	(18)	(19)	(20)	(21)
021754.80+000234.0	2.044	19.07	6	9.17	0.22	-	0.37	0.46	0.82	4E-3	-0.77	0.07	0.82	0.04	-0.88	0.02	-0.65	0.15	0.60	0.20
022111.89+010548.8	1.487	17.76	7	9.35	0.24	-	0.35	0.43	-	-	0.10	0.81	-	-	-0.57	0.18	-	-	0.39	0.38
022143.19-001803.8	2.621	18.89	7	9.64	0.19	-	0.21	0.64	0.92	2E-3	-	-	0.42	0.33	-	-	0.92	2E-3	-	-
022157.81+000042.5	1.041	18.39	7	9.53	0.04	-	-0.07	0.87	-	-	0.89	6E-3	-	-	0.07	0.87	-	-	-0.14	0.75
022230.28+001844.5	2.191	19.04	7	9.32	0.15	-	-0.39	0.38	-0.61	0.14	0.00	1.00	-0.53	0.21	0.11	0.82	-0.85	0.01	0.64	0.12
022246.46-004836.1	1.541	17.28	7	9.10	0.81	-	0.36	0.43	-	-	0.67	0.09	-	-	-0.35	0.43	-	-	-0.03	0.93
022321.38-000733.8	1.534	19.00	6	8.96	0.28	-	0.08	0.87	-	-	0.71	0.11	-	-	0.03	0.96	-	-	0.82	0.04
022400.23-001241.3	1.571	20.01	7	8.96	0.10	-	-0.82	0.04	-0.02	0.95	0.60	0.21	-0.42	0.39	-0.14	0.78	0.08	0.87	0.60	0.20
022430.17-004131.1	1.669	18.94	6	9.24	0.13	-	0.25	0.62	-0.25	0.62	-0.14	0.78	-0.31	0.54	-0.31	0.54	0.94	4E-3	0.77	0.07
022518.36-001332.3	3.628	19.18	11	9.36	0.38	-	0.61	0.04	0.26	0.43	-	-	-0.29	0.37	-	-	-0.06	0.85	-	-
022554.85+005451.9	2.969	18.65	15	8.98	1.10	-	0.09	0.73	0.33	0.22	-	-	-0.33	0.21	-	-	0.33	0.22	-	-
022826.69-003802.3	1.515	18.24	8	9.48	0.16	-	0.11	0.77	-	-	0.45	0.26	-	-	-0.12	0.78	-	-	0.19	0.65
022844.09+000217.0	2.706	17.87	15	9.46	0.47	-	-0.66	0.01	0.02	0.92	-	-	-0.47	0.10	-	-	0.02	0.92	-	-
025754.18+000506.4	2.679	19.17	8	9.96	0.07	89.7	0.26	0.53	0.35	0.38	-	-	0.23	0.57	-	-	0.00	1.00	-	-
030551.14-000557.3	0.839	19.21	10	8.36	0.36	-	-0.75	0.01	-	-	-0.18	0.63	-	-	-0.67	0.04	-	-	0.00	1.00
030719.91+004538.7	1.903	19.00	9	8.93	0.39	-	0.06	0.86	0.73	0.02	0.13	0.73	0.46	0.20	-0.70	0.03	0.67	0.04	0.48	0.18
030815.84+010721.4	1.217	18.80	9	8.45	0.60	-	0.10	0.79	-	-	0.69	0.03	-	-	0.53	0.13	-	-	0.48	0.18
030905.37+005808.9	1.518	19.21	7	9.11	0.15	-	-0.11	0.77	-	-	-0.61	0.14	-	-	-0.75	0.05	-	-	0.53	0.21
030907.49+002419.0	2.083	18.88	8	9.76	0.08	-	0.66	0.07	0.42	0.28	0.42	0.28	0.28	0.49	0.35	0.36	0.40	0.32	0.14	0.74
031003.01-004645.7	2.115	17.74	9	9.19	1.20	-	0.56	0.11	0.16	0.66	0.51	0.15	-0.45	0.22	0.26	0.48	0.31	0.41	0.96	2E-5
031019.95+010111.5	1.389	17.56	9	9.58	0.22	-	-0.20	0.60	-	-	0.85	3E-3	-	-	0.48	0.19	-	-	0.41	0.26
031028.87-005326.2	2.443	18.43	9	9.74	0.22	-	-0.25	0.51	0.19	0.61	-	-	0.01	0.96	-	-	-0.40	0.28	-	-
031030.90+000517.6	1.229	19.50	9	8.51	0.36	-	-0.18	0.63	-	-	0.06	0.86	-	-	0.11	0.76	-	-	0.56	0.11
031036.84+005521.7	3.783	19.50	9	9.90	0.15	-	0.40	0.28	-0.01	0.96	-	-	-0.13	0.73	-	-	-0.01	0.96	-	-
031037.63+004008.9	1.273	18.67	8	9.04	0.14	-	-0.59	0.11	-	-	0.59	0.11	-	-	-0.35	0.38	-	-	0.02	0.95

Table 3—Continued

Object (SDSS J)	z	i	N	log M_{bh}	$\dot{m}$	R	L_{con} - α_λ		L_{con} - $L_{C_{IV}}$		L_{con} - L_{MgII}		L_{con} - $EW_{C_{IV}}$		L_{con} - EW_{MgII}		$L_{C_{IV}}$ - FWHM		L_{MgII} - FWHM	
		(mag)		($M_\odot$)			r	p	r	p	r	p	r	p	r	p	r	p	r	p
(1)	(2)	(3)	(4)	(5)	(6)	(7)	(8)	(9)	(10)	(11)	(12)	(13)	(14)	(15)	(16)	(17)	(18)	(19)	(20)	(21)
031118.52+002437.0	0.863	18.19	8	8.71	0.30	-	-0.32	0.48	-	-	-0.46	0.29	-	-	-0.75	0.05	-	-	-0.07	0.87
031127.55+005357.4	1.764	18.90	9	9.38	0.12	-	0.39	0.38	0.21	0.64	-0.28	0.53	-0.03	0.93	-0.46	0.29	-0.07	0.88	0.67	0.09
031129.29+005638.6	1.507	19.35	8	9.29	0.09	45.3	-0.78	0.01	-	-	0.08	0.83	-	-	-0.43	0.24	-	-	0.24	0.51
031131.41-002127.4	1.572	19.35	6	9.71	0.09	-	-0.23	0.57	0.42	0.28	0.14	0.73	0.26	0.53	-0.52	0.18	0.95	2E-4	0.40	0.31
031156.45-004157.0	0.955	19.35	9	9.15	0.06	-	-0.33	0.41	-	-	0.19	0.65	-	-	-0.92	8E-4	-	-	0.09	0.82
031227.13-003446.2	1.776	18.88	10	9.52	0.08	-	-0.28	0.42	0.34	0.32	0.41	0.37	0.16	0.65	0.46	0.17	0.26	0.47	0.72	0.01
031237.56+004511.3	1.822	19.03	9	9.49	0.09	-	-0.16	0.66	0.64	0.05	0.38	0.30	-0.31	0.40	-0.37	0.34	-0.15	0.70	0.36	0.33
031246.45-005024.6	1.581	18.75	9	9.16	0.22	-	0.40	0.28	0.19	0.61	0.53	0.13	0.24	0.51	0.33	0.38	0.48	0.18	0.39	0.28
031307.92-003221.9	1.411	19.04	8	8.89	0.23	-	-0.13	0.75	-	-	-0.19	0.64	-	-	-0.53	0.17	-	-	0.90	2E-3
031318.66+003623.9	1.256	18.07	10	10.02	0.03	221.9	-0.68	0.02	-	-	-0.45	0.18	-	-	-0.45	0.18	-	-	0.97	1E-6
031343.07-001623.4	1.562	19.32	10	9.19	0.12	-	-0.09	0.80	0.50	0.13	0.91	2E-4	0.23	0.51	0.49	0.45	0.53	0.11	-0.04	0.90
031348.34-010433.0	2.468	18.99	9	9.03	0.60	-	0.35	0.35	0.54	0.12	-	-	0.44	0.22	-	-	0.54	0.12	-	-
031404.44-003947.3	2.105	18.51	9	9.80	0.12	-	0.46	0.20	0.34	0.35	0.78	0.01	0.23	0.54	0.03	0.92	0.00	1.00	0.10	0.79
031439.08-000249.3	1.152	18.77	8	8.65	0.28	-	0.59	0.11	-	-	0.50	0.20	-	-	-0.67	0.07	-	-	0.80	0.01
031444.54-005701.1	1.506	18.33	9	9.43	0.14	-	0.05	0.89	-	-	0.31	0.40	-	-	-0.26	0.48	-	-	0.14	0.70
031452.06+001346.3	3.202	19.27	8	8.77	1.73	66.4	-0.65	0.15	0.14	0.78	-	-	-0.25	0.62	-	-	0.14	0.78	-	-
031645.55-000553.3	1.397	19.33	8	9.72	0.03	18.4	-0.6	0.14	-	-	0.00	1.00	-	-	-0.28	0.53	-	-	0.73	0.06
032933.97-004801.0	1.878	18.83	6	9.07	0.46	-	-0.77	0.07	0.88	0.02	0.48	0.32	0.60	0.21	-0.02	0.96	-0.43	0.39	0.94	4E-3

Note. — The quasars at $z > 0.8$ in our sample: Col. (1) object name; Col. (2) redshift; Col. (3) i-band apparent magnitude; Col. (4) number of spectroscopic observations; Col. (5) black hole mass; Col. (6) Eddington ratio, defined as L_{bol}/L_{Edd}; Col. (7) radio loudness, $R = f_{6cm}/f_{2500}$; Cols. (8) - (21) the Spearman rank correlation coefficients and probability level for L_{con} - α_λ, L_{con} - $L_{C_{IV}}$, L_{con} - L_{MgII}, L_{con} - $EW_{C_{IV}}$, L_{con} - EW_{MgII}, $L_{C_{IV}}$ - FWHM, and L_{MgII} - FWHM.